Topological Antiferromagnetic Van der Waals Phase in Topological Insulator/Ferromagnet Heterostructures Synthesized by a CMOS-Compatible Sputtering Technique

Nirjhar Bhattacharjee[1], Krishnamurthy Mahalingam[2], Adrian Fedorko[3], Valeria Lauter[4], Matthew Matzelle[3], Bahadur Singh[5], Alexander Grutter[6], Alexandria Will-Cole[1], Michael Page[2], Michael McConney[2], Robert Markiewicz[3], Arun Bansil[3], Don Heiman[3,7], and Nian Xiang Sun[1]

[1] Northeastern University, Department of Electrical and Computer Engineering Boston, MA
[2] Air Force Research Laboratory, Nano-electronic Materials Branch Wright Patterson Air Force Base Boston, OH
[3] Northeastern University, Department of Physics Boston, MA
[4] Quantum Condensed Matter Division Neutron Sciences Directorate, Oak Ridge National Laboratory Boston, TN 37831, USA
[5] Tata Institute of Fundamental Research, Department of Condensed Matter Physics and Materials Science Mumbai 400005, India
[6] NIST Center for Neutron Research, National Institute of Standards and Technology Gaithersburg, MD
[7] Plasma Science and Fusion Center MIT, Cambridge, MA

Abstract

Breaking time-reversal symmetry by introducing magnetic order, thereby opening a gap in the topological surface state bands, is essential for realizing useful topological properties such as the quantum anomalous Hall and axion insulator states. In this work, a novel topological antiferromagnetic (AFM) phase is created at the interface of a sputtered, *c*-axis-oriented, topological insulator/ferromagnet heterostructure—$Bi_2Te_3/Ni_{80}Fe_{20}$ because of diffusion of Ni in Bi_2Te_3 (Ni-Bi_2Te_3). The AFM property of the Ni-Bi_2Te_3 interfacial layer is established by observation of spontaneous exchange bias in the magnetic hysteresis loop and compensated moments in the depth profile of the magnetization using polarized neutron reflectometry. Analysis of the structural and chemical properties of the Ni-Bi_2Te_3 layer is carried out using selected-area electron diffraction, electron energy loss spectroscopy, and X-ray photoelectron spectroscopy. These studies, in parallel with first-principles calculations, indicate a solid-state chemical reaction that leads to the formation of Ni−Te bonds and the presence of topological antiferromagnetic (AFM) compound $NiBi_2Te_4$ in the Ni-Bi_2Te_3 interface layer. The Neél temperature of the Ni-Bi_2Te_3 layer is ≈63 K, which is higher than that of typical magnetic topological insulators (MTIs). The presented results provide a pathway toward industrial complementary metal−oxide−semiconductor (CMOS)-process-

compatible sputtered-MTI heterostructures, leading to novel materials for topological quantum devices.

Keywords
ferromagnets, interface, magnetic topological insulators, topological insulators, van der Waals materials

1. Introduction

Magnetic order in topological insulators (TIs) and breaking of time-reversal symmetry[1,2] has been achieved through magnetic doping of TIs,[3–11] magnetic proximity effect,[12–18] and synthesis of intrinsic magnetic TI (MTI) compounds such as, $MnBi_2Te_4$ that supports the quantum anomalous Hall (QAH) state at low temperatures.[19–28] These exotic quantum states can help realize topological quantum computers and energy-efficient spintronic devices. Introducing impurity atoms in TIs can also lead to the emergence of new phases with exotic properties, such as superconductivity.[29] TIs in van der Waals (vdW) materials are promising systems in this connection due to the tunability and diversity of their optical, electronic, and magnetic properties. Recently, TI thin films have been shown to form new material phases at the interface when coupled with metallic thin films[30–32] resulting from the diffusion of elements. Notably, an AFM order in TIs in these interfacial material phases has not been reported. Much of these existing experimental works have been performed on *c*-axis-oriented Bi_2Se_3-based systems. However, theoretical calculations have shown an order of magnitude larger superexchange interaction strength in Te-based TI material systems compared to those based on Se,[19,20] making the latter more promising for creating topological magnetic materials.

TI thin films grown using magnetron sputtering have been reported recently as promising candidates for energy-efficient spintronic devices.[33–37] Sputtering is the semiconductor industry's accepted manufacturing process for growing thin films with high film quality, large throughput, and ability for large area uniform thin film deposition. However, high-quality *c*-axis ordering in sputter-deposited TIs has been elusive, which is required for realizing the topological properties. This has prevented the study of many fascinating materials phases emerging in heterostructure interfaces and also has hindered the integration of TI-based spintronic devices in industrial complementary metal–oxide–semiconductor (CMOS) processes.

Here, the discovery of a vdW antiferromagnetic (AFM) phase of $NiBi_2Te_4$ at the Ni-Bi_2Te_3 interface, which emerges as a distinct interfacial layer when a highly *c*-axis-oriented Bi_2Te_3 thin film is coupled with the ferromagetic (FM) alloy, $Ni_{80}Fe_{20}$ (Py) as a result of the diffusion of Ni into Bi_2Te_3. Growth of the Py layer following Bi_2Te_3 growth is carried out in

the same sputtering chamber without breaking vacuum. This ensures access to a topologically nontrivial surface of Bi_2Te_3 for the creation of the AFM Ni-Bi_2Te_3 layer. Measurements of the magnetic hysteresis loops show the appearance of a large spontaneous exchange bias (EB), signaling an AFM phase in proximity to the FM layer of Py having substantial exchange interaction between the AFM–FM layers.[38–45] The location of the AFM order in the interface of the Bi_2Te_3/Py heterostructure was confirmed using polarized neutron reflectometry (PNR) experiments. In addition, using selected-area electron diffraction (SAED) we observed new diffraction peaks emerging in the AFM Ni-Bi_2Te_3 layer, in addition to the Bi_2Te_3 peaks signaling the appearance of new planes along the crystalline *c*-axis. Analysis of the diffraction peaks provided strong evidence of presence of the AFM TI compound $NiBi_2Te_4$ in the interfacial Ni-Bi_2Te_3 layer along with other disordered materials phases (Section 9, Supporting Information). Using electron energy loss spectroscopy (EELS) and X-ray photoelectron spectroscopy (XPS), we identified changes in electronic binding energies (BE) of Ni,Te and Bi[46–48] in the AFM Ni-Bi_2Te_3 layer. These experimental results demonstrate the formation of Ni–chalcogenides: Ni–Te bonds with Ni^{2+} oxidation state. The experimental results, along with first-principles density functional theory (DFT) calculations, strongly point toward the AFM topological compound $NiBiTe_4$[19,20,50–53] as the most likely candidate contributing to AFM order in the Ni-Bi_2Te_3 layer. The Neél temperature of the Ni-Bi_2Te_3 layer was measured to be ≈63 K, which is higher than MTIs reported in the literature.[54]

2. Results and Discussion

2.1 Characterization of Crystal Structure and Interface Morphology

Heterostructures were grown by depositing 40 nm of *c*-axis-oriented crystalline-textured Bi_2Te_3 on thermally oxidized Si/SiO_2 substrates using RF magnetron sputtering, followed by a 20 nm layer of Py (see Experimental Section for details). Reference samples were prepared with Bi_2Te_3 (40 nm)/TiO_x (3 nm) for X-ray diffraction (XRD) analysis. The wide-angle XRD plot in Figure 1a clearly shows the Bi_2Te_3 phase with a significant crystalline orientation along the *c*-axis. The surface roughness of the Bi_2Te_3 layer was measured to be ≈1 nm using X-ray reflectivity (Figure S1, Supporting Information) for the Bi_2Te_3/TiO_x sample. This value of surface roughness is typical of sputter-grown thin films. These results show that high-quality, *c*-axis-oriented, crystalline-ordered TI can be grown using sputtering on an amorphous substrate, enabling us to study the interface phases in TI/FM heterostructures.

The microstructure of the interface was studied extensively using several techniques. High-resolution transmission electron microscopy (HRTEM) was used to image the cross-section of the Bi_2Te_3/Py heterostructure, as shown in Figure 1b. Four distinct layers are identified: Bi_2Te_3, Ni-Bi_2Te_3, Py* (Ni-depleted Py), and Py. The HRTEM and scanning transmission

electron microscopy–high-angle annular dark-field (STEM-HAADF) images in Figure 1b,c clearly show vdW layers, which confirms the crystalline-textured, *c*-axis-oriented growth of the Bi_2Te_3 thin film. Energy-dispersive X-ray spectroscopy (EDS) was used to characterize the elemental composition of the heterostructure as presented in Table 1 (details of analysis in Figure S4, Supporting Information). The obtained Bi:Te ratio of 2:3 confirms a stoichiometric composition of the sputtered Bi_2Te_3 thin film. It is important to note that a significant diffusion of Ni occurs within the interface, as illustrated in the normalized EDS depth profile in Figure 1d. This diffusion of Ni is accompanied by a substantial loss of magnetic moment, $\boldsymbol{m}$, by ≈40% compared to a control sample of Py as shown in the room temperature $\boldsymbol{m}$(H) loop in Figure 1d. The consistence of this significant moment loss is further verified using the PNR measurements (Section7, Supporting Information). The diffused Ni in Bi_2Te_3 undergoes a solid-state chemical reaction, possibly catalyzed by the topological surface state (TSS) electrons.[27,55] A second interface layer also forms because of depletion of Ni from Py, wherein trace amounts of Bi and Te are also detected, which is referred to as the Py* layer. The 5 nm thick Ni-Bi_2Te_3 AFM layer is clearly a vdW material phase which is evident from the STEM-HAADF image in Figure 1b,c and will be further verified using several techniques.

2.2 Exchange Bias due to FM/AFM Interaction

To study the magnetic properties in the sputter-deposited Bi_2Te_3/Py heterostructure, $\boldsymbol{m}$(H) loop measurements were carried out with the field in the plane of the sample with a superconducting quantum interference device (SQUID) magnetometer. As expected, the in-plane hysteresis loops measured at room temperature, T = 300 K are centered with a small coercive field, $\mu_0 H_c \approx 0.5$ mT, which is comparable to the Py control sample in Figure 1e. In contrast, the zero-field-cooled (ZFC) and field-cooled (FC) low-temperature measurements exhibit a sizable spontaneous EB along with a significant enhancement of $\mu_0 H_c$, as shown in Figure 2a. This EB shift and $\mu_0 H_c$ enhancement is a characteristic of a large exchange interaction in the FM/AFM interface.[40–43] A high energy of the exchange interaction between the FM and AFM layers not only shifts the loop $\boldsymbol{m}$(H) loop along the axis of the *H*-field (exchange bias), but often also leads to an increase in coercive field.[40,41] This possibly happens due to the pinning of domains in a magnetic frustrated interface. The ZFC $\boldsymbol{m}$(H) loop measured at 6 K is shifted by 8 mT off-center and an enhanced coercive field was determined to be $\mu_o H_c = 9.5$ mT. FC hysteresis loops were also measured where the samples were cooled with an applied field of ± 1 T. As shown in Figure 2b, EB field switched from -18.0 mT to +18.0 mT for FC of +1 T and -1 T, respectively. This confirms the presence of a large exchange coupling that exists between the FM, Py, and the AFM, Ni-Bi_2Te_3 layers, with a large in-plane magnetic anisotropy[45] indicative of a vdW layered A-type AFM[19,20] material (more evidence of A-type AFM order in Section S8, Supporting Information). The

Neél temperature at which the AFM phase emerges was obtained from ***m***(T) measurements performed in both FC and ZFC conditions using a constant applied field of 5 mT as shown in Figure 2c,d. Figure 2d plots the derivative, d***m***/d*T* of the ZFC ***m***(T), showing a sharp peak at 63 K, which is the Neél transition temperature of the AFM phase.[42,43] This Neél temperature of the Ni-Bi_2Te_3 AFM phase is higher than the transition temperatures of MTIs reported in the literature.[54]

2.3 Confirmation of AFM Order in Ni-Bi_2Te_3 Layer Using PNR

The location of the layer with AFM ordering in the Ni-Bi_2Te_3 layer present in the heterostructure was confirmed by performing depth-sensitive PNR measurements[56,57] at the Oak Ridge National Laboratory (ORNL) Spallation Neutron Source using the MagRef reflectometer.[58] The experiments were performed at T = 7 K under ZFC conditions using 1 T and 5 mT applied fields. The theoretical model was fit to the PNR profiles using Refl1D software for the reflectivity and spin-asymmetry experimental data, SA = $(R^+ - R^-)/(R^+ + R^-)$ as shown in Figure 3a,b. The structural and magnetic depth profiles were parameterized using the nuclear and magnetic scattering length densities (NSLD and MSLD, respectively) as shown in Figure 3c (full PNR profile in Figure S7, Supporting Information). The NSLD and MSLD depth profiles obtained from the fit to the reflectivity represent the structural and magnetic depth profiles of the heterostructure, respectively. Note that the reduction in NSLD by $\approx 2 \times 10^{-6}$ Å^{-2} in the Py* layer is compensated by a gain in NSLD by approximately the same value in the Ni-Bi_2Te_3 layer. This suggests that the Ni lost by the Py in the Py* layer forms the distinct Ni-Bi_2Te_3 interfacial layer, which is in agreement with the STEM-HAADF image in Figure 1c.

For the applied field of 1 T, most of the moment vectors are aligned along the field direction, including the moments in the interfacial layer, illustrated in Figure 3d. But at a low applied field of 5 mT, the AFM order in the Ni-Bi_2Te_3 vdW layers yields largely compensated moments. From the MSLD depth profile in Figure 3c, the Ni-Bi_2Te_3 layer was observed to have an order of magnitude larger value of 0.26×10^{-6} Å^{-2} at 1 T compared to 0.034×10^{-6} Å^{-2} at 5 mT. The reduction in the value of moments by an order of magnitude at a low applied field confirms the AFM ordering in the Ni-Bi_2Te_3 interfacial layer. A lower value of MSLD can also mean that the moments are oriented out of the film plane, as PNR is insensitive to the perpendicular component of moments. However, the large exchange bias for in-plane ***m***(H) loop measurements as shown in Figure 2 and significantly low remnant magnetization in out-of-plane ***m***(H) loop measurement (Figure S7, Supporting Information) provides clear evidence of largely in-plane easy-axis AFM order in the Ni-Bi_2Te_3 layer with small canting of moments out-of-plane.

2.4 Evidence of Topologically Nontrivial Compounds in AFM Ni-Bi_2Te_3 Phase

The *c*-axis crystalline-oriented texture of the vdW-layered Bi_2Te_3 and the Ni-Bi_2Te_3 AFM layers are clearly identified in the HRTEM and STEM-HAADF images in Figure 1b,c and SAED patterns in Figure 4a–c. In order to understand the structural and chemical properties of the Ni-Bi_2Te_3 layer, SAED followed by cross-section EELS and depth-dependent XPS measurements were performed. These measurements provide strong evidence of formation of topologically nontrivial vdW compounds in the AFM Ni-Bi_2Te_3 layer as a result of diffusion and solid-state reaction between the diffused Ni and Bi_2Te_3.

The SAED measurements clearly demonstrate a vdW-layered structure in the Ni-Bi_2Te_3 layer as shown by the single line of diffraction spots in Figure 4a, as well as in the Bi_2Te_3 of Figure 4b. Figure 4c contains the diffraction intensities extracted from Figure 4a,b, for both the Bi_2Te_3 and Ni-Bi_2Te_3 layers, where additional peaks emerge in the Ni-Bi_2Te_3 layer compared to the peaks representing quintuple layers (QL) of Bi_2Te_3. These additional diffraction peaks confirm formation of new planes parallel to the crystalline *c*-axis and support the diffusion of Ni and reaction with Bi_2Te_3. A similar pattern of the SAED peaks in the Ni-Bi_2Te_3 layer compared to the Bi_2Te_3 layer further confirms the vdW nature of the Ni-Bi_2Te_3 layer. These key pieces of information are strong indications of the formation of a Ni-based vdW-layered magnetic topological material phase in the interfacial Ni-Bi_2Te_3 layer. Theoretical calculations of $NiBi_2Te_4$, which belongs to the MBi_2Te_4 (M = Mn, Ni, V, Eu etc.) family, have shown it to be an intrinsic MTI compound with large exchange energy.[19,20] With this in mind, the emergence of a large exchange-bias from the AFM-ordered Ni-Bi_2Te_3 layer points toward the emergence of Ni-based AFM phases with topologically nontrivial properties. Qualitative comparison of the positions of the *c*-axis-oriented SAED peaks with theoretical diffraction peak positions of possible Ni, Bi, and Te based vdW materials, raises the possibility of the presence of topologically nontrivial compounds such as $NiBi_2Te_4$, $(Ni,Bi)_2Te_3$, NiTe, and $NiTe_2$ in the Ni-Bi_2Te_3 AFM layer.[19,20,52] Of these, however, NiTe and $NiTe_2$ are known to be paramagnetic.[48] This makes the topological magnetic compounds, $NiBi_2Te_4$ and $(Ni,Bi)_2Te_3$ (substitution of Bi sites by Ni) highly probable candidates for the AFM ordering in the Ni-Bi_2Te_3 layer. The average *c*-axis length was calculated as 40.63 Å from the SAED data of the $NiBi_2Te_3$ layer which is close to the theoretical value of 41.01 Å for $NiBi_2Te_4$. This further supports the presence of the MTI compound $NiBi_2Te_4$ in the Ni-Bi_2Te_3 layer making it the most likely candidate for the AFM order in the layer (Section 9, Supporting Information). The presence of a few diffraction peaks that deviat beyond the measurement error limits of SAED in Figure 4c (also Figure S10a,d, Supporting Information) also suggests presence of other materials phases in addition to Bi_2Te_3 and $NiBi_2Te_4$ in the Ni-Bi_2Te_3 layer. Presence of disorder and resultant diffraction peak shifts and broadening is however expected in such an interfacial layer formed by diffusion and solid-state reaction between Ni and Bi_2Te_3.

Further evidence supporting the formation of compounds in the AFM Ni-Bi_2Te_3 layer is provided by cross-sectional EELS and depth-dependent XPS measurements, shown in Figure 4d–g. The EELS measurements for core shell electrons were performed on the layers marked in the STEM-HAADF cross-section images shown in Figure 1c. For the Ni-Bi_2Te_3 layer, Figure 4d shows new pre-edge features emerging at 30 eV lower binding energies (BE) prior to Ni and Fe L-shell edges, which were absent for the Py reference layer. In addition to these pre-edge features, a change in L3:L2 peak ratio of Ni from 1.90 in the Py layer to 1.41 in the Ni-Bi_2Te_3 layer was observed. It is concluded that the emergence of the pre-edge features and reduction in L_3:L_2 peaks ratio can be attributed to the increase in valence state of Ni from a metallic state in Py toward Ni^{2+} oxidation state in the Ni-Bi_2Te_3 layer.[46,47] It is also noted that the Fe L-shell peaks showed reduction in L_3:L_2 ratio from 1.94 in the Py region to 1.25 in the Ni-Bi_2Te_3 layer. However, Fe in the Ni-Bi_2Te_3 layer has a much lower concentration of ≈4.1% compared to ≈39.4% for Ni as determined by EDX. Hence, the AFM phase should be predominantly attributed to Ni-based compounds in the Ni-Bi_2Te_3 layer.

Figure 4e compares the normalized XPS spectra of Ni in the Py reference and the interfacial Ni-Bi_2Te_3 layers. The satellite peak at 858.7 eV shifts by ≈1 eV to higher BE, which is a signature of Ni–chalcogenide (Ni–Te) bonds.[48] Similarly, a large shift of ≈1 eV is also observed in the Fe $2p_3$ binding energies (Figure S6, Supporting Information). Further, as shown in Figure 4f,g and Table 2, the Te $3d_5$ and Bi 4f peaks also experience a shift of ≈0.5 eV from 572.8 eV and ≈0.3 eV from 157.4 eV (main peak positions) toward higher and lower binding energies, respectively, in the Ni-Bi_2Te_3 layer compared to the reference layer of Bi_2Te_3. The shift in XPS peaks for Ni, Te, and Bi suggest Ni–Te–Bi bonds in the AFM Ni-Bi_2Te_3 layer leading to the formation of compounds.

Detailed first-principles calculations based on the DFT framework were carried out to identify the possible candidates contributing to the AFM order in the Ni-Bi_2Te_3 layer (Section 10, Supporting Information). The formation energies of several possible compounds composed of Ni, Bi, and Te were compared, such as Ni intercalated within vdW gaps of Bi_2Te_3, substitution of Ni in Bi sites to form $(Ni,Bi)_2Te_3$, and the MTI compound $NiBi_2Te_4$, both against well-known stable compounds and with each other. The calculated formation energies of the possible Ni, Bi and Te based compounds (Section 10, Supporting Information) along with the SAED peak positions shown in Figure 4 suggests the compound, $NiBi_2Te_4$ as the most probable candidate contributing to the AFM order in the Ni-Bi_2Te_3 layer. Our careful band structure calculations (Section 11, Supporting Information) established $NiBi_2Te_4$ as an MTI compound with a bulk band inversion and nontrivial Z_4 topological number of 2. The existence of diffraction peaks corresponding to Bi_2Te_3 QL along with the additional peaks in the AFM Ni-Bi_2Te_3 layer as shown in Figure 4c, also points toward presence of multilayers of (Ni,Bi)2Te3 and/or Bi_2Te_3 along with $NiBi_2Te_4$[25] and possibly other materials phases. In such vdW-layered AFM systems, the magnetic

ordering is usually dictated by superexchange interactions.[19,20] The magnetic monolayers are FM ordered within the vdW plane, but each plane is coupled by RKKY exchange in the out-of-plane direction, giving rise to an A-type AFM ordering.[19,20,49–51] Of further interest is the high Neél transition temperature of 63 K measured for the Ni-Bi_2Te_3 AFM layer, which is higher than the MTIs[54] reported in literature. This makes the present Ni-Bi_2Te_3 phase an appealing candidate for high-temperature QAH and other topological phases that are required for realizing energy-efficient spintronics and topological quantum computing applications.

3. Conclusion

Sputtered TI/FM heterostructures of highly *c*-axis-oriented Bi_2Te_3 coupled with the FM alloy Py were shown to exhibit a large exchange bias field at low temperatures that arise from the emergence of a novel AFM phase in the vdW Ni-Bi_2Te_3 layer in the interface. The Bi_2Te_3/ $Ni_{80}Fe_{20}$ heterostructures were grown on amorphous thermally oxidized Si substrates. Using PNR measurements, the AFM ordering in the Ni-Bi_2Te_3 layer was confirmed. The diffused Ni undergoes a solid-state reaction with Bi_2Te_3, which is believed to be catalyzed by delocalized TSS electrons of the Bi_2Te_3. SAED diffraction patterns for the Ni-Bi_2Te_3 layer exhibited new peaks in addition to the Bi_2Te_3 QL peaks, confirming the formation of additional planes oriented along the crystalline *c*-axis. Furthermore, using cross-section EELS and depth-dependent XPS measurements, spectral changes were observed for Ni, Fe, Bi, and Te in the Ni-Bi_2Te_3 layer, as compared to the reference Bi_2Te_3 and Py layers. These are attributed to the formation of Ni–Te bonds in the interface layer. Comparison of diffraction data and the detection of Ni–Te bonds provide strong experimental evidence of presence of AFM TI compound, $NiBi_2Te_4$ in the interfacial Ni-Bi_2Te_3 layer. Using first principles DFT calculations, the $NiBi_2Te_4$ compound was found as the most likely candidate contributing to the AFM order in the Ni-Bi_2Te_3 layer. Band structure calculations determined the $NiBi_2Te_4$ compound to be topological with a Z4 topological number of 2. Furthermore, the ≈63 K Neél transition temperature of the Ni-Bi_2Te_3 phase is considerably higher than the magnetic transition temperatures of recent experimentally synthesized MTIs, which makes the present interfacial phase in sputtered TI/FM heterostructures promising candidates for high-temperature QAH and other topological quantum devices. These results open the path for further exploration of industrial CMOS compatible sputter-grown TIs and TI/FM material systems for high-temperature topological material systems and the realization of energy-efficient topological spintronic devices.

4. Experimental Section

Material Growth: Heterostructures of 30 nm Bi_2Te_3 were grown by co-sputtering a composite Bi_2Te_3 target with a Te target using RF magnetron sputtering at 90 W and 20 W, respectively,

with 4 mTorr (0.53 Pa) Ar pressure on thermally oxidized Si substrates. The base pressure of the sputtering chamber was <2 × 10^{-7} Torr (2.67 × 10^{-5} Pa). The samples were grown with substrates maintained at 250 °C. Samples were further annealed inside the chamber at 45 mTorr (6 Pa) Ar pressure for 25 min at 250 °C to achieve high-quality crystalline *c*-axis-oriented textured growth. The samples were cooled to room temperature in a high vacuum for ≈5 h before deposition of other layers. For the magnetic sampless, 20 nm Py and 3 nm Ti capping layer were deposited at room temperature after deposition of Bi_2Te_3. The Ti layer subsequently oxidized to TiO_x on exposure to atmosphere.

XRD Characterization: XRD was collected by using a background-free, highly collimated beam of CuKα1 radiation (wavelength λ = 1.54056 Å) on the sample surface. The collection of X-ray scattering intensity was performed by a 2D charged-coupled device (CCD). The Bragg reflections were indexed according to the Bi_2Te_3 bulk hexagonal unit cell. The *x*-axis in Figure 1a was indexed in terms of the hexagonal unit cell of the Bi_2Te_3, as indicated by (h, k, $-(h+k)$, l) where h, k, and l are the Miller indices. A highly *c*-axis-oriented growth (along (0,0,3l) direction) of Bi_2Te_3 was identified using XRD.

TEM, EELS, and XEDS Characterization: Samples for TEM investigations were prepared by focused ion beam (FIB) milling using a Ga^+ ion source. Prior to TEM observation an additional cleaning procedure was performed by Ar-ion milling to reduce surface amorphous layer and residual Ga due to the FIB process. The TEM observations were performed using a Talos 200-FX (ThermoFiszher Scientific Inc.) TEM operated at an acceleration voltage of 200 kV. XEDS measurements were performed using the ChemiSTEM (ThermoFisher Scientific) technology and acquisition and processing of the spectra was performed by spectrum imaging technique using the Esprit 1.9 (Brucker Inc.) software. The Nanobeam diffraction (Figure 4a,b) and STEM/EELS (Figure 4c) studies were performed using an aberration-corrected (image) Titan operated at an accelerating voltage of 200 kV. The EELS data acquisition was performed using a GIF-Quantum (Gatan, Inc) spectrometer and processed using the DigitalMicrograph 2.10 (Gatan, Inc.) software.

Hysteresis Loop Measurements: Magnetization $m(H)$ and $m(T)$ measurements were obtained using a Quantum Design superconducting quantum interference device (SQUID) magnetometer. Hystersis loop $\boldsymbol{m}(H)$ measurements were carried out at various temperatures between 6 and 300 K. The ZFC and FC $\boldsymbol{m}$(T) measurements were obtained while increasing the temperature in an applied field of 5 mT, and FC measurements were performed after cooling the sample under an applied field of 1 T. Room-temperature $\boldsymbol{m}(H)$ measurements in Figure 1e were taken using a vibrating sample magnetometer (VSM).

PNR Characterization: PNR experiments were carried out on the Magnetism Reflectometer at the Spallation Neutron Source at Oak Ridge National Laboratory.[58] A neutron beam with

a wavelength band of 2.6–8.6 Å and a high polarization of 98.5% was used. Measurements were performed in a closed cycle refrigerator in an applied external magnetic field using a Bruker electromagnet with a maximum magnetic field of 1 T. In the time-of-flight method, a collimated polychromatic beam of polarized neutrons with a wavelength band $\Delta\lambda$ impinges on the film at a grazing incidence angle θ. The neutrons interact in the film with atomic nuclei and the spins of unpaired electrons.[59,60] The reflected intensity was measured as a function of wave vector transfer, $Q = 4\pi\sin(\theta)/\lambda$, for two neutron polarizations R^+ and R^-, with the neutron spin parallel (+) or antiparallel (–) to the direction of the external field, H_{ext}. To separate nuclear from magnetic scattering, the data were presented in the form of the spin–asymmetry ratio $SA = (R^+ - R^-)/(R^+ + R^-)$ as shown in Figure 3b and Figure S7b, Supporting Information), where SA = 0 indicates that there no magnetic moment in the system. Electrically neutral, spin-polarized neutrons penetrate the entire structure of the film and generate a depth profile of magnetic and structural composition of the film interfaces down to the substrate with a resolution of 0.5 nm. The depth profiles of the nuclear and magnetic scattering length densities (NSLD and MSLD) correspond to the depth profile of the chemical and in-plane magnetization vector distributions on the atomic scale, respectively.[58–60] Based on these neutron scattering merits, PNR serves as the powerful technique to simultaneously and nondestructively characterize chemical and magnetic nature of buried interfaces.[58] Neutron scattering measurements were performed on a 2 × 2 cm^2 surface samples.

XPS Depth Profile: Valence state of elements near the surface of the sample was characterized using a PHI Versaprobe II X-ray photoelectron spectrometer with a scanning monochromated Al source (1486.6 eV, 100 W, spot size 200 µm). The instrument's C_{60}^+ ion source was used to perform depth profiling. A takeoff angle of 45° between the sample surface and analyzer was used. The X-ray beam collected Ni2p, Fe2p, Te3d, and Bi4f elemental information whilst rastering over a 200 × 1400 μm^2 area. Sputtering occurred in 1 min intervals, while the sample was moved using concentric Zalar rotation at 0.10 rad s^{-1}. The operation power of the C_{60}^+ source was maintained at 1 kV and 0.5 µA and rastered over a 2 × 2 mm^2 area at an angle 70° to the surface normal. Valence states of elements were determined by comparing the shift in XPS peaks in BE, and the relative sensitivity factors were provided in PHI's Multipak processing software. Background-subtraction and smoothing of the data were performed using a five-point quadratic Savitzky−Golay algorithm. The relative position of the layers was based on amplitude of the spectra and relative shift in peak positions. Spectra peaks were fit in CasaXPS, and data were plotted and analyzed using Matlab.

Acknowledgements
This work was partially supported by the U.S Army under grant no. W911NF20P0009, the NIH Award UF1NS107694, and the NSF TANMS ERC Award 1160504. The work of D.H.

and A.F. was partially supported by the National Science Foundation grant DMR-1905661 and the Air Force Office of Scientific Research award FA9550-20-1-0247. The work of M.M. and A.B. was supported by the US Department of Energy (DOE), Office of Science, Basic Energy Sciences Grant No. DE-SC0019275 and of R.M. by DOE grant number DE-FG02-07ER46352, and benefited from Northeastern University's Advanced Scientific Computation Center and the Discovery Cluster, and the National Energy Research Scientific Computing Center through DOE Grant No. DE-AC02-05CH11231. The work of K.M. was supported by Air Force Research Laboratory under AFRL/NEMO contract: FA8650-19-F-5403 TO3. Studies employing the Titan 60–300 TEM were performed at the Center for Electron Microscopy and Analysis (CEMAS) at The Ohio State University with support through Air Force contract FA8650-18-2-5295. The work at TIFR Mumbai was supported by the Department of Atomic Energy of the Government of India under Project No. 12-R&D-TFR-5.10-0100. A portion of this research used resources at the Spallation Neutron Source, a DOE Office of Science User Facility operated by the Oak Ridge National Laboratory. The authors thank Charles Settens and Libby Shaw (MIT, Materials Research Laboratory) for help with XRD and XPS measurements. Certain commercial equipments are identified in this paper to foster understanding. Such identification does not imply recommendation or endorsement by Northeastern University, AFRL, ORNL, NIST, and TIFR.

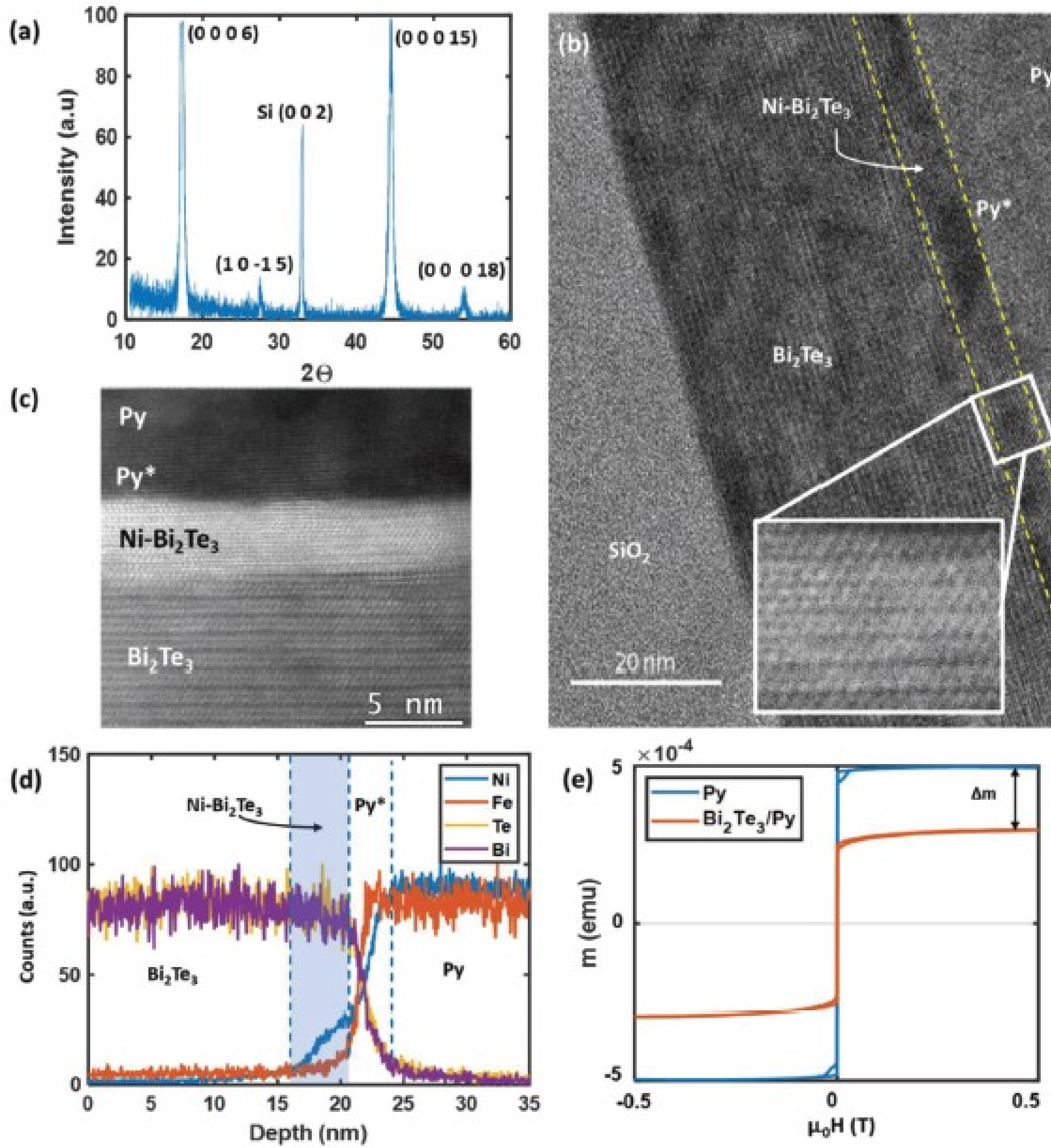

Figure 1. a) Wide-angle XRD intensity versus 2θ showing *c*-axis orientation of Bi_2Te_3 film on Si substrate. b) HRTEM image of sputtered Bi_2Te_3/Py heterostructure with interface layers labeled. Inset: Expanded image of Ni-Bi_2Te_3 layer showing vdW layered structure. c) STEM-HAADF image of sputtered Bi_2Te_3/Py heterostructure showing clear atomically aligned vdW layered Ni-Bi_2Te_3 interface formation d) Depth profile of elements in the heterostructure measured using EDS. The Ni-Bi_2Te_3 interfacial layer is highlighted in blue color. e) Room temperature $\boldsymbol{m}(H)$ loops showing loss of moments in the Bi_2Te_3/Py compared to the control sample of Py with identical deposited Py thickness and film area. 1 emu = 1 mA m^2.

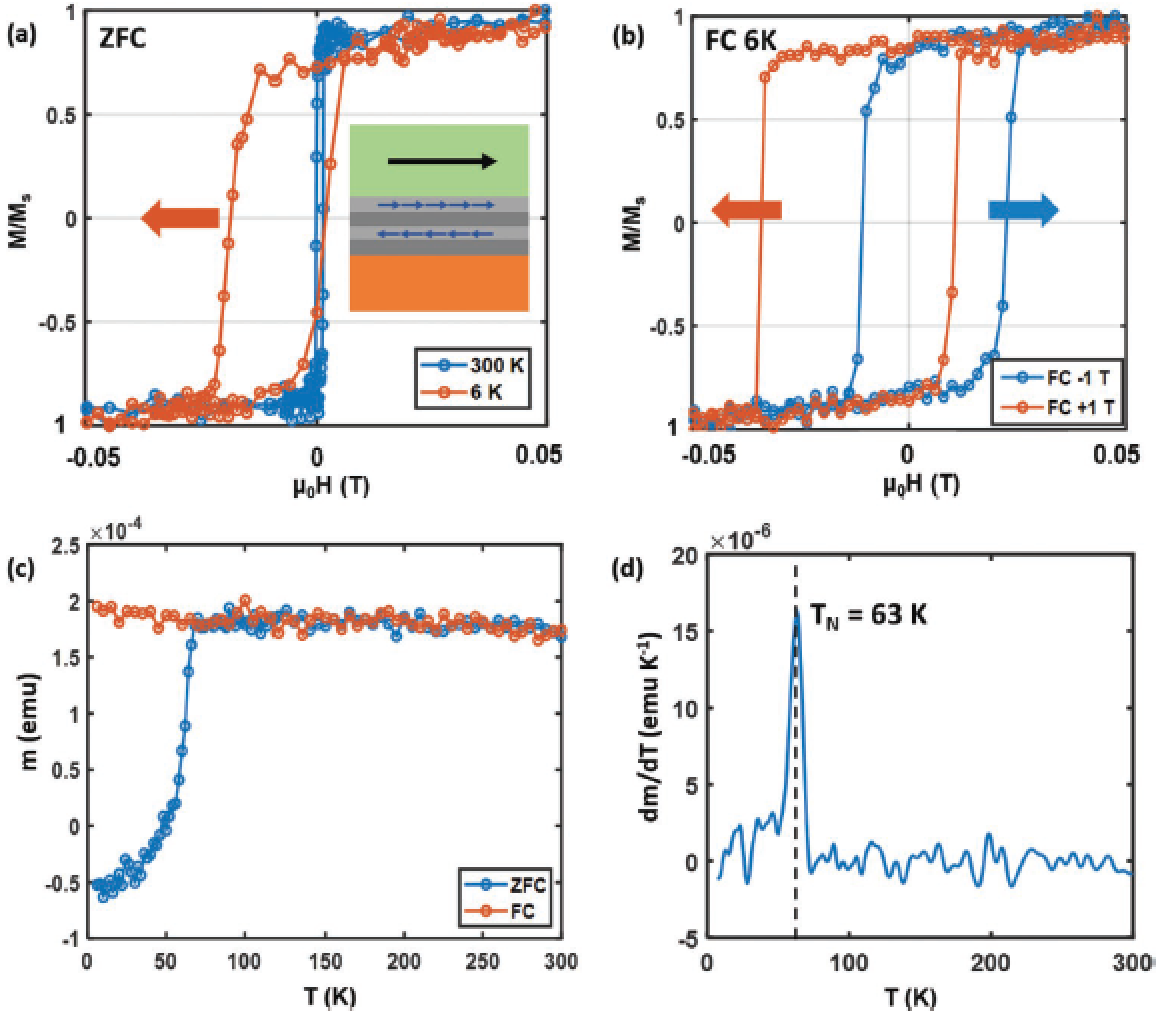

Figure 2. a) ZFC hysteresis loops at 300 and 6 K showing exchange bias at low temperature. b) Hysteresis loops for FC at −1 T and +1 T showing switching of EB. c) ZFC and FC $\boldsymbol{m}(T)$ plots measured at 5 mT applied field. d) Derivative, d$\boldsymbol{m}$/dT, of the ZFC plot in Figure 2c showing a peak at ≈63 K corresponding to the Néel temperature of the AFM phase.

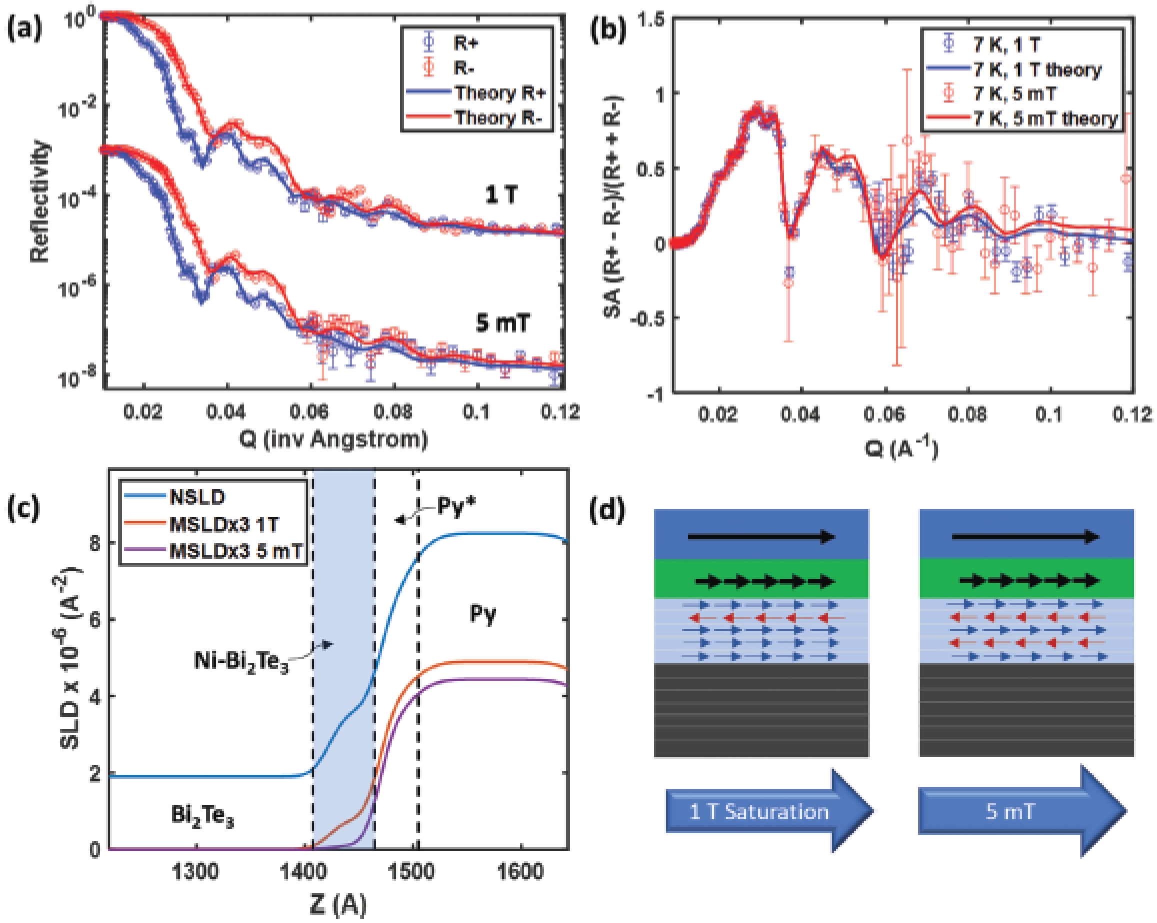

Figure 3. a) PNR reflectivity plots for measurements at 1 T and 5 mT with fits for the theoretical model. b) SA plots derived from (a) for raw data and model fitting. (The error bars represent the standard deviation). c) MSLD × 3 and NSLD depth profiles of showing the AFM phase emerging in the Ni-Bi_2Te_3 interfacial layer. The AFM Ni-Bi_2Te_3 layer is highlighted in blue. d) Schematic illustrations of the orientation of magnetic moments across the layers (bottom to top: Bi_2Te_3 in black, Ni-Bi_2Te_3 in light blue, Ni depleted Py* layer in green, Py in deep blue) at 1 T saturation field and 5 mT low field (not to scale). All these measurements were performed at a temperature of 7 K in ZFC condition.

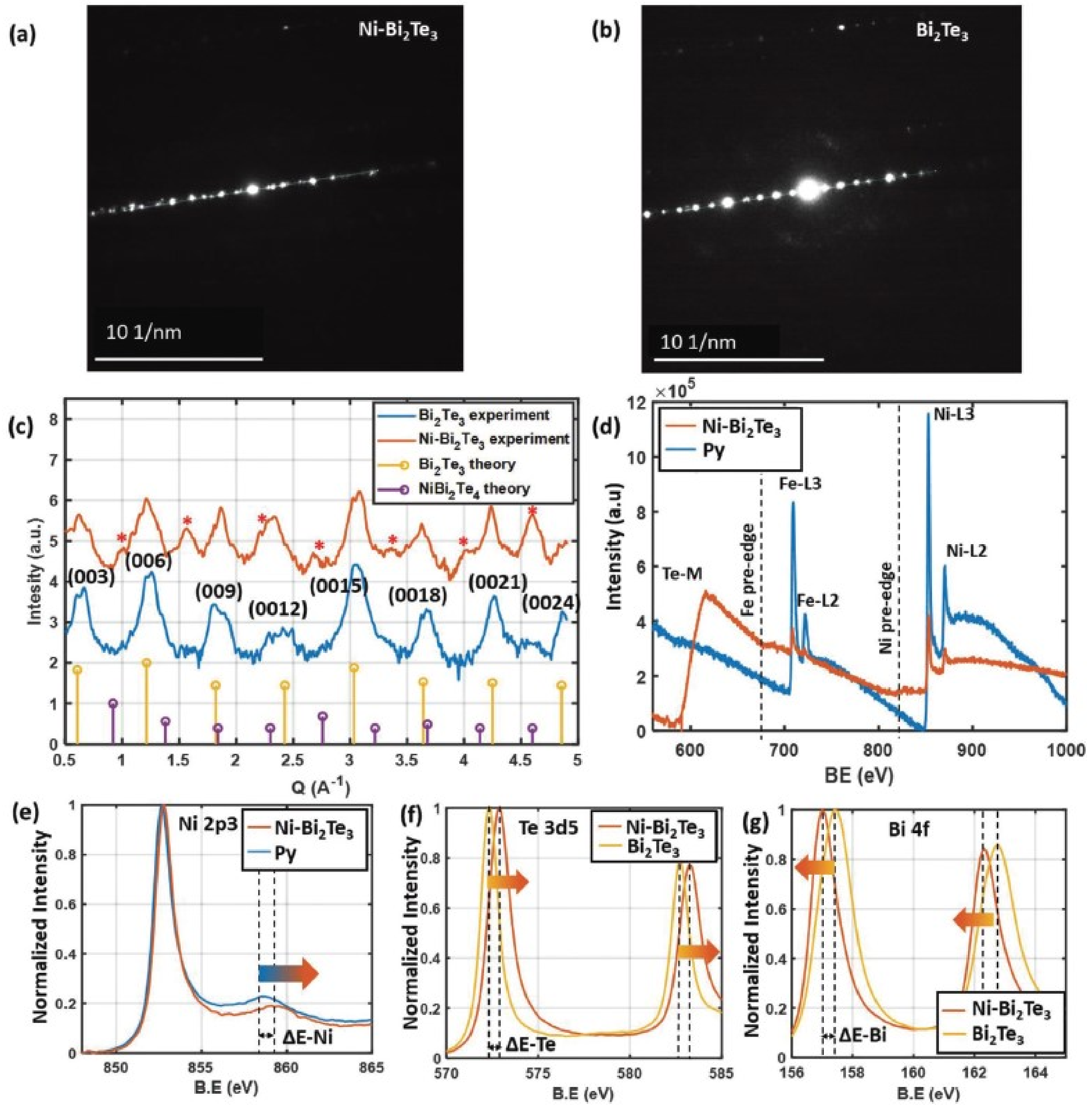

Figure 4. a,b) SAED intensity for sputtered Bi_2Te_3/Py from STEM-HAADF image in Figure 1c showing diffraction peaks at Ni-Bi_2Te_3 (a) and Bi_2Te_3 (b) regions. c) SAED peak positions versus Q extracted from (a,b) for Bi_2Te_3 (blue) and Ni-Bi_2Te_3 (orange) layers. The new peaks emerging in the Ni-Bi_2Te_3 layer are marked with a red "*." The bottom vertical graphs show theoretical c-axis diffraction peaks of Bi_2Te_3 (yellow) and $NiBi_2Te_4$ (purple) extracted from cif files. d) EELS spectra for Te M-shell and Fe, Ni L-shell electrons corresponding to sputtered Bi_2Te_3/Py heterostructure interface layer cross section showing new pre-edges and reduced L3:L2 ratios for Ni and Fe in the Ni-Bi_2Te_3 region compared to the Py reference region corresponding to STEM-HAADF image in Figure 1c. e−g) Normalized XPS spectra

for: e) Ni 2p3/2 showing shift in satellite peak by 1 eV toward higher BE; f) Te 3d5/2 showing 0.5 eV shift toward higher BE; and g) Bi 4f showing 0.3 eV shift toward lower BE.

Table 1. Atomic % of the Bi2Te3/Ni-Bi2Te3/Py*/Py heterostructure shown in Figure 1. The numbers in parantheses represent their standard deviation in each layer.

Element	**Bi_2Te_3 [%]**	**Ni-Bi_2Te_3 [%]**	**Py* [%]**	**Py [%]**
Bi	39.03 (5.17)	22.25 (4.05)	3.21 (1.05)	0.03 (0.05)
Te	60.28 (4.87)	34.31(3.82)	5.24 (1.04)	0.20 (0.07)
Ni	0.38 (0.03)	39.38 (0.63)	69.90 (1.89)	80.79 (2.47)
Fe	0.31 (0.03)	4.11 (0.09)	21.65 (0.58)	18.99 (0.58)

Table 2. XPS peak positions in units of eV of interest for Ni, Fe, Bi, and Te for Ni-Bi_2Te_3 layer compared to reference Py and Bi_2Te_3 layers.

Element	**Py [eV]**	**Ni-Bi_2Te_3 [eV]**	**Bi_2Te_3 [eV]**	**ΔE [eV]**
Ni	858.7	859.6	–	0.9
Fe	712.1	713.0	–	0.9
Te	–	572.8	572.3	0.5
Bi	–	157.1	157.4	−0.3

References

1. F. D. M. Haldane, Phys. Rev. Lett. 1988, 61, 2015
2. R. Yu, W. Zhang, H. J. Zhang, S. C. Zhang, X. Dai, Z. Fanvg, Science 2010, 329, 61.
3. C. Z. Chang, J. Zhang, X. Feng, J. Shen, Z. Zhang, M. Guo, K. Li, Y. Ou, P. Wei, L.-L. Wang, Z.-Q. Ji, Y. Feng, S. Ji, X. Chen, J. Jia, X. Dai, Z. Fang, S.-C. Zhang, K. He, Y. Wang, L. Lu, X.-C. Ma, Q.-K. Xue, Science 2013, 340, 167.
4. C. Z. Chang, W. Zhao, D. Y. Kim, H. Zhang, B. A. Assaf, D. Heiman, S.-C. Zhang, C. Liu, M. H. Chan, J. S. Moodera, Nat. Mater. 2015, 14, 473.
5. Y. Tokura, K. Yasuda, A. Tsukazaki, Nat. Rev. Phys. 2019, 1, 126.
6. C. Liu, Y. Wang, H. Li, Y. Wu, Y. Li, J. Li, K. He, Y. Xu, J. Zhang, Y. Wang, Nat. Mater. 2020, 19, 522.
7. W. Wang, Y. Ou, C. Liu, Y. Wang, K. He, Q. K. Xue, W. Wu, Nat. Phys. 2018, 14, 791.
8. J. Teng, N. Liu, Y. Li, J. Semicond. 2019, 40, 081507.
9. A. Tcakaev, V. B. Zabolotnyy, R. J. Green, T. R. F. Peixoto, F. Stier, M. Dettbarn, S. Schreyeck, M. Winnerlein, R. C. Vidal, S. Schatz, H. B. Vasili, M. Valvidares, K. Brunner, C. Gould, H. Bentmann, F. Reinert, L. W. Molenkamp, V. Hinkov, Phys. Rev. B 2020, 101, 045127.
10. A. Tcakaev, V. B. Zabolotnyy, C. I. Fornari, P. Rüßmann, T. R. F. Peixoto, F. Stier, M. Dettbarn, P. Kagerer, E. Weschke, E. Schierle, P. Bencok, P. H. O. Rappl, E. Abramof, H. Bentmann, E. Goering, F. Reinert, V. Hinkov, Phys. Rev. B 2020, 102, 184401
11. Y. Ni, Z. Zhang, I. C. Nlebedim, R. L. Hadimani, G. Tuttle, D. C. Jiles, J. Appl. Phys. 2015, 117, 17C748.
12. F. Katmis, V. Lauter, F. S. Nogueira, B. A. Assaf, M. E. Jamer, P. Wei, B. Satpati, J. W. Freeland, I. Eremin, D. Heiman, P. Jarillo-Herrero, J. S. Moodera, Nature 2016, 533, 513.
13. X. Che, K. Murata, L. Pan, Q. L. He, G. Yu, Q. Shao, G. Yin, P. Deng, Y. Fan, B. Ma, X. Liang, B. Zhang, X. Han, L. Bi, Q. H. Yang, H. Zhang, K. L. Wang, ACS Nano 2018, 12, 5042.
14. C. Lee, F. Katmis, P. Jarillo-Herrero, J. S. Moodera, N. Gedik, Nat. Commun. 2016, 7, 12014.
15. W. Y. Choi, J. H. Jeon, H. W. Bang, W. Yoo, S. K. Jerng, S. H. Chun, S. Lee, M. H. Jung, Adv. Quantum Technol. 2021, 4, 2000124.
16. J. A. Hutasoit, T. D. Stanescu, Phys. Rev. B 2011, 84, 085103.
17. J. M. Marmolejo-Tejada, K. Dolui, P. Lazić, P. H. Chang, S. Smidstrup, D. Stradi, K. Stokbro, B. K. Nikolic, Nano Lett. 2017, 17, 5626.
18. I. Zutic, A. Matos-Abiague, B. Scharf, H. Dery, K. Belashchenko, Mater. Today 2019, 22, 85.

19. J. Li, Y. Li, S. Du, Z. Wang, B. L. Gu, S. C. Zhang, K. He, W. Duan, Y. Xu, Sci. Adv. 2019, 5, eaaw5685.
20. Z. Li, J. Li, K. He, X. Wan, W. Duan, Y. Xu, Phys. Rev. B 2020, 102, 081107(R).
21. Y. Lia, Y. Xu, Comp. Mater. Sci. 2021, 190, 110262
22. H. Fu, C.-X. Liu, B. Yan, Sci. Adv. 2020, 6, eaaz0948
23. Y. Gong, J. Guo, J. Li, K. Zhu, M. Liao, X. Liu, Q. Zhang, L. Gu, L. Tang, X. Feng, D. Zhang, W. Li, C. Song, L. Wang, P. Yu, X. Chen, H. Y. Y. Wang, W. Duan, Y. Xu, S. C. Zhang, X. Ma, Q. K. Xue, K. He, Chin. Phys. Lett. 2019, 36, 076801.
24. M. Z. Shi, B. Lei, C. S. Zhu, D. H. Ma, J. H. Cui, Z. L. Sun, J. J. Ying, X. H. Chen, Phys. Rev. B 2019, 100, 155144.
25. E. D. L. Rienks, S. Wimmer, J. S. Barriga, O. Caha, P. S. Mandal, J. Růžička, A. Ney, H. Steiner, V. V. Volobuev, H. Groiss, M. Albu, G. Kothleitner, Nature 2019, 576, 423
26. J. Wu, F. Liu, M. Sasase, K. Ienaga, Y. Obata, R. Yukawa, K. Horiba, H. Kumigashira, S. Okuma, T. Inoshita, H. Hosono, Sci. Adv. 2019, 5, eaax9989.
27. Y. Deng, Y. Yu, M. Z. Shi, Z. Guo, Z. Xu, J. Wang, X. H. Chen, Y. Zhang, Science 2020, 367, 895.
28. H. Deng, Z. Chen, A. Wołoś, M. Konczykowski, K. Sobczak, J. Sitnicka, I. V. Fedorchenko, J. Borysiuk, T. Heider, Ł. Pluciński, K. Park, A. B. Georgescu, J. Cano, L. K. Elbaum, Nat. Phys. 2021, 17, 36.
29. Y. S. Hor, A. J. Williams, J. G. Checkelsky, P. Roushan, J. Seo, Q. Xu, H. W. Zandbergen, A. Yazdani, N. P. Ong, R. J. Cava, Phys. Rev. Lett. 2010, 104, 057001.
30. S. J. Chang, P. Y. Chuang, C. W. Chong, Y. J. Chen, J. C. A. Huang, P. W. Chene, Y. C. Tseng, RSC Adv. 2018, 8, 7785.
31. L. A. Walsh, C. M. Smyth, C. L. Hinkle, J. Phys. Chem. C 2017, 121, 23551.
32. K. Ferfolja, M. Fanetti, S. Gardonio, M. Panighel, I. Pis, S. Nappini, M. Valant, J. Mater. Chem. C 2020, 8, 11492.
33. M. DC, R. Grassi, J. Y. Chen, M. Jamali, D. R. Hickey, D. Zhang, Z. Zhao, H. Li, P. Quarterman, Y. Lv, M. Li, A. Manchon, K. A. Mkhoyan, T. Low, J. P. Wang, Nat. Mater. 2018, 17, 800.
34. M. DC, T. Liu, J. Y. Chen, T. Peterson, P. Sahu, H. Li, Z. Zhao, M. Wu, J. P. Wang, Appl. Phys. Lett. 2019, 114, 102401.
35. Q. Guo, Y. Wu, L. Xu, Y. Gong, Y. Ou, Y. Liu, L. Li, Y. Yan, G. Han, D. Wang, L. Wang, S. Long, B. Zhang, X. Cao, S. Yang, X. Wang, Y. Huang, T. Liu, G. Yu, K. He, J. Teng, Chin. Phys. Lett. 2020, 37, 057301.
36.
    a. Q. X. Guo, Z. X. Ren, Y. Y. Huang, Z. C. Zheng, X. M. Wang, W. Hw, Z. D. Zhu, J. Teng, Chin. Phys. B 2021, 30, 067307;
    b. T. Y. Chen, C. W. Peng, C. F. Pai, ACS Appl. Mater. Interfaces 2020, 12,

7788.
37. J. A. Thornton, J. Vac. Sci. Technol. 1974, 11, 666.
38. R. L. Stamps, J. Phys. D: Appl. Phys. 2000, 33, R247
39. J. Saha, R. H. Victora, Phys. Rev. B 2007, 76, 100405(R)
40. J. K. Murthy, P. S. Anil Kumar, Sci. Rep. 2017, 7, 6919
41. C. Leighton, J. Nogués, B. J. Jönsson-Åkerman, I. K. Schuller, Phys. Rev. Lett. 2000, 84, 3466.
42. T. Maity, S. Goswami, D. Bhattacharya, S. Roy, Phys. Rev. Lett. 2013, 110, 107201.
43. J. Liu, A. Singh, Y. Yang, F. Liu, A. Ionescu, B. Kuerbanjiang, C. H. W. Barnes, T. Hesjedal, Nano Lett. 2020, 20, 5315.
44. W. B. Rui, Y. Hu, A. Du, M. W. X. B. You, W. Zhang, S. M. Zhou, J. Du, Sci. Rep. 2015, 5, 13640.
45. R. J. O. Mossanek, G. Dominguez-Canizares, A. Gutierrez, M. Abbate, D. Diaz-Fernandez, L. Soriano, J. Phys.: Condens. Matter 2013, 25, 495506.
46. Z. L. Wang, J. S. Yin, Y. D. Jiang, Micron 2000, 31, 571
47. H. W. Nesbitt, D. Legrand, G. M. Bancroft, Phys. Chem. Miner. 2000, 27, 357.
48. Q. Mao, Y. Zhang, Q. Chen, R. Li, X. Geng, J. Yang, H. Hao, M. Fang, Phys. Status Solidi B 2020, 257, 1900224.
49. C. Xu, B. Li, W. Jiao, W. Zhou, B. Qian, R. Sankar, N. D. Zhigadlo, Y. Qi, D. Qian, F. C. Chou, X. Xu, Chem. Mater. 2018, 30, 4823.
50. M. Aras, C. Kilic, S. Ciraci, Phys. Rev. B 2020, 101, 054429.
51. B. Ghosh, D. Mondal, C. N. Kuo, C. S. Lue, J. Nayak, J. Fujii, Vobornik, A. Politano, A. Agarwal, Phys. Rev. B 2019, 100, 195134.
52. M. Eschbach, M. Lanius, C. Niu, E. Młyńczak, P. Gospodarič, J. Kellner, P. Schüffelgen, M. Gehlmann, S. Döring, E. Neumann, M. Luysberg, G. Mussler, L. Plucinski, M. Morgenstern, Grützmacher, G. Bihlmayer, S. Blügel, C. M. Schneider, Nat. Commun. 2017, 8, 14976.
53. A. Mauger, C. Godart, Phys. Rep. 1986, 141, 51.
54. S. Wimmer, J. Sánchez-Barriga, P. Küppers, A. Ney, E. Schierle, F. Freyse, O. Caha, J. Michalicka, M. Liebmann, D. Primetzhofer, M. Hoffmann, A. Ernst, M. M. Otrokov, G. Bihlmayer, E. Weschke, B. Lake, E. V. Chulkov, M. Morgenstern, G. Bauer, G. Springholz, O. Rader, Adv. Mater. 2021, 33, 2102935.
55. G. Li, C. Felser, Appl. Phys. Lett. 2020, 116, 070501.
56. S. Blundell, M. Gester, J. Bland, H. Lauter, V. Pasyuk, A. Petrenko, Phys. Rev. B 1995, 51, 9395.
57. V. Lauter-Pasyuk, Collection SFN 2007, 7, s221.
58. V. Lauter, H. Ambaye, R. Goyette, W.-T. H. Lee, A. Parizzi, Phys. B 2009, 404, 2543.
59. V. Lauter-Pasyuk, H. Lauter, B. Toperverg, O. Nikonov, E. Kravtsov, M. Milyaev, L.

Romashev, V. Ustinov, Phys. B 2000, 283, 194
60. H. Zabel, K. Theis-Bröhl, B. P. Toperverg, Handbook of Magnetism and Advanced Magnetic Materials, Vol. 12, Wiley, New York 2007, p. 1237.